EARTHQUAKE RESPONSE OF BURIED STRUCTURES AND LIFELINES: EFFECTS OF FAULT SOURCE PARAMETERS

Alireza Farahani [1], Anil C. Wijeyewickrema [2], Tatsuo Ohmachi [3]

1) Post Doctoral Researcher, CUEE, farahani.a.aa@m.titech.ac.jp
2) Associate Professor, Department of Civil Engineering, wijeyewickrema.a.aa@m.titech.ac.jp
3) Professor, Department of Built Environment, ohmachi@enveng.titech.ac.jp

1. Introduction

This study concerns simulation of dynamic fault rupturing in semi-infinite media and its effects on transient response of underground structures and consists of two parts. In the first part, there is no tunnel and the medium consists of a layered elastic half-space. The responses of the top layer to different fault source parameters are investigated. In the second part, the medium is a homogeneous elastic half-space where a circular concrete tunnel exists. The internal forces and deformations of the tunnel for different fault source parameters are investigated to reveal the parameters which have a major influence on the failure of a circular tunnel when it is located close to the fault line.

In order to apply dynamic rupturing forces to the system, the split-node technique (Melosh and Raefsky, 1981) is used to introduce relative slip in the adjacent elements on the opposite sides of the fault line (Appendix).

2. Effects of fault source parameters on the response of a layered medium

There are three kinds of numerical methods to simulate fault rupturing in the ground, finite difference, finite element and meshfree methods. Among them, meshfree method produces more accurate results. In finite element method, one of the efficient and practical methods to introduce fault slip is the split-node technique which is difficult to be incorporated into meshfree method. The purpose of this research is to model surface soft soil layers by meshfree technique (Liu and Gu, 2001, 2005) and obtain the response of the ground surface for different values of fault source parameters. In order to apply fault dislocation beneath the meshfree region, the combined finite element-meshfree method is utilized in which the fault slip is introduced in the lower layer finite element area (Fig 2.1). At the boundaries of the truncated model, simple dashpots have been used to reduce reflection of the outgoing waves back into the system (Lysmer and Kuhlmeyer, 1969).

The fault source parameters which are considered during the parametric studies are dip-slip angle θ, rupture velocity V_{rup}, rise time of the fault slip T_0, final depth of the fault tip from bottom of upper layer C, fault propagation direction, permanent slip δ, and fault width W. Among these parameters, permanent slip $\delta = 2$ m and fault width $W = 15000$ m are identical in all cases to keep the released energy constant. The effects of rigidity ratio between layers $\Gamma = G_h / G_s$ and thickness of the upper soft layer H on the surface response are investigated as well, where G_h is the shear modulus of half-space and G_s is the shear modulus of superficial layer. For all cases, horizontal and vertical displacements at different horizontal distances to the vertical projection of the final fault tip on the ground surface (D_t) are calculated.

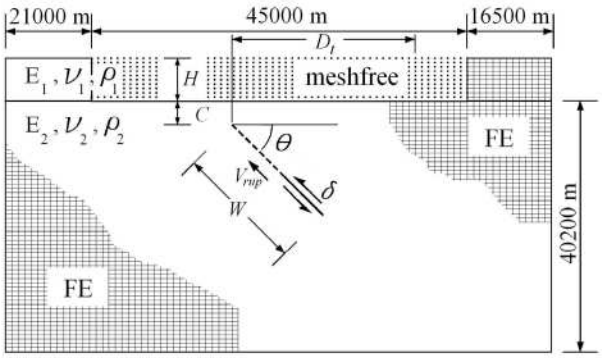

Fig. 2.1. Geometry of the medium consists of elastic half-space (FEM) overlain by elastic layer (meshfree).

Table 2.1 shows material properties of the layers where E is Young's modulus (N/m^2), ν is Poisson's ratio and ρ is mass density of layers (kg/m^3).

Table 2.1
Material properties of the half-space and soft surface layer for different rigidity ratios.

Property	$\Gamma = 1$	$\Gamma = 2$	$\Gamma = 4$
E_1	7.490E10	3.745E10	1.872E10
E_2	7.490E10	7.490E10	7.490E10
$\nu_1 = \nu_2$	0.27	0.27	0.27
ρ_1	2600	2300	2000
ρ_2	2600	2600	2600

In all cases, default values for parameters are considered as follows unless they are expressed explicitly:

$\delta = 2$ m, $W = 15000$ m, $\theta = 45^\circ$, $\Gamma = 4$, $V_{rup}/V_s = 0.7$, $T_0 = 1$ sec, $C = 2700$ m, $H = 5000$ m, fault propagation direction is unilateral.

Table 2.2 shows the values of fault source parameters in each case.

Table 2.2
Values for each fault source parameter.

Case No.	Values
1	$\theta = 30^\circ,\ 45^\circ,\ 60^\circ,\ 75^\circ,\ 90^\circ$
2	$\Gamma = 1,\ 2,\ 4$
3	$V_{rup}/V_s = 0.6,\ 0.7,\ 0.8,\ 0.9$
4	$T_0 = 1,\ 2,\ 4$ sec
5	$C = 0,\ 1200,\ 2700$ m
6	$H = 1000,\ 3000,\ 5000$ m
7	Unilateral, Bilateral

2.1. Dip-slip angle (case 1)

Figures 2.2 and 2.3 show the horizontal and vertical displacement of the soft layer surface at different locations for different dip-slip angles.

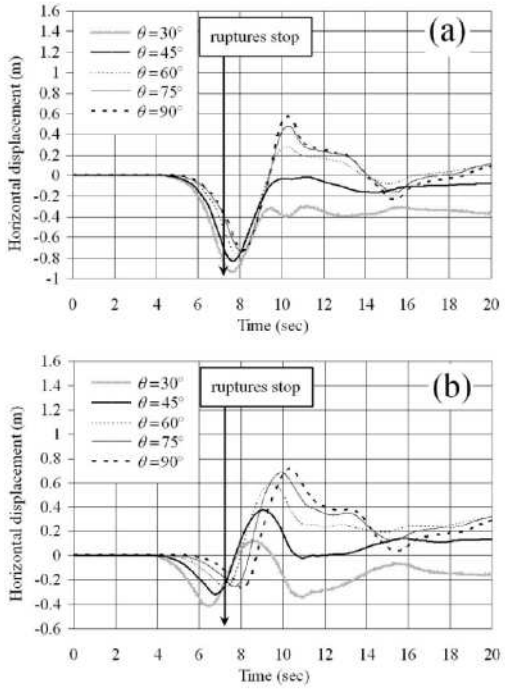

Fig. 2.2. Horizontal ground surface displacement for different dip-slip angles for (a) $D_t = 300$ m; (b) $D_t = 5000$ m. Arrow indicates the time ruptures end.

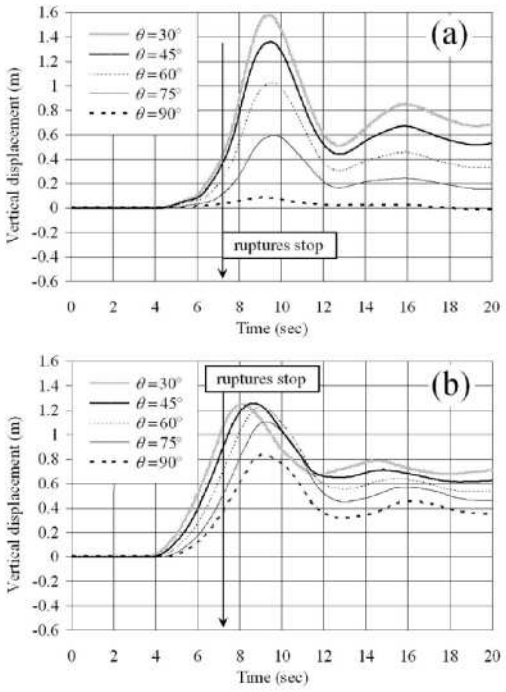

Fig. 2.3. Vertical ground surface displacement for different dip-slip angles for (a) $D_t = 300$ m; (b) $D_t = 5000$ m. Arrow indicates the time ruptures end.

2.2. Rigidity ratio (case 2)

Figures 2.4 and 2.5 show the horizontal and vertical displacement of the soft layer surface at different locations for different rigidity ratio between half-space and upper soft layer.

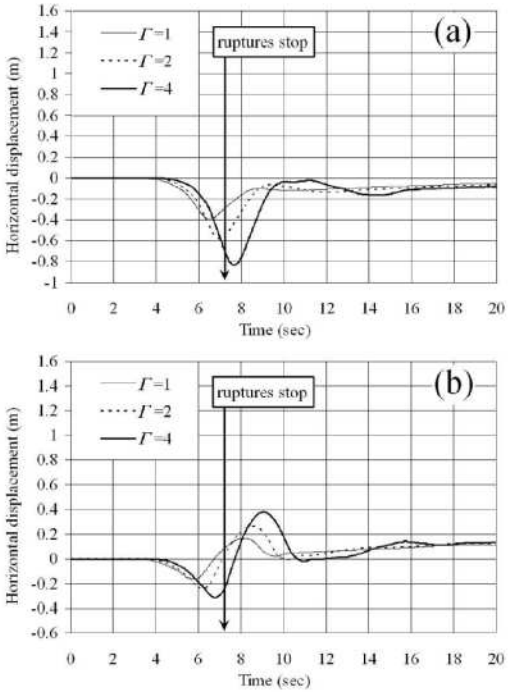

Fig. 2.4. Horizontal ground surface displacement for different rigidity ratios for (a) $D_t = 300$ m; (b) $D_t = 5000$ m. Arrow indicates the time ruptures end.

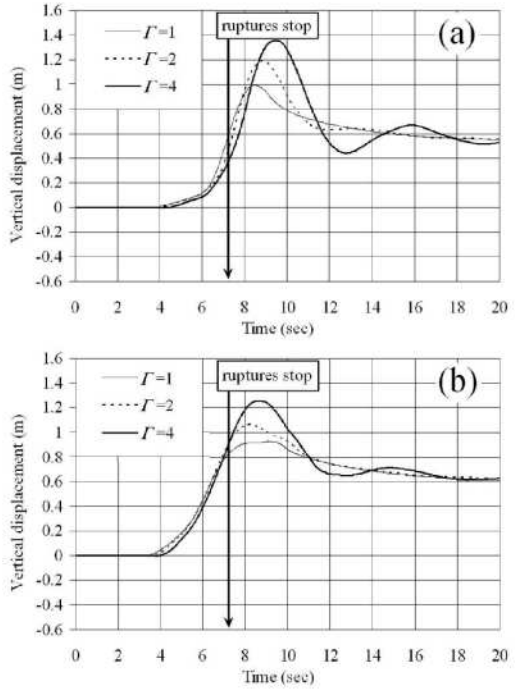

Fig. 2.5. Vertical ground surface displacement for different rigidity ratios for (a) D_t = 300 m; (b) D_t = 5000 m. Arrow indicates the time ruptures end.

2.3. Rupture velocity (case 3)

Figures 2.6 and 2.7 show the horizontal and vertical displacement of the soft layer surface at different locations for different rupture velocities.

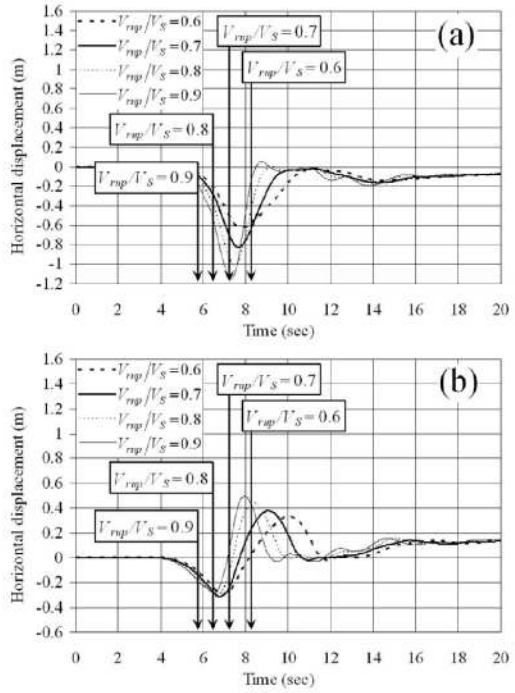

Fig. 2.6. Horizontal ground surface displacement for different rupture velocities for (a) D_t = 300 m; (b) D_t = 5000 m. Arrows indicate the times ruptures end.

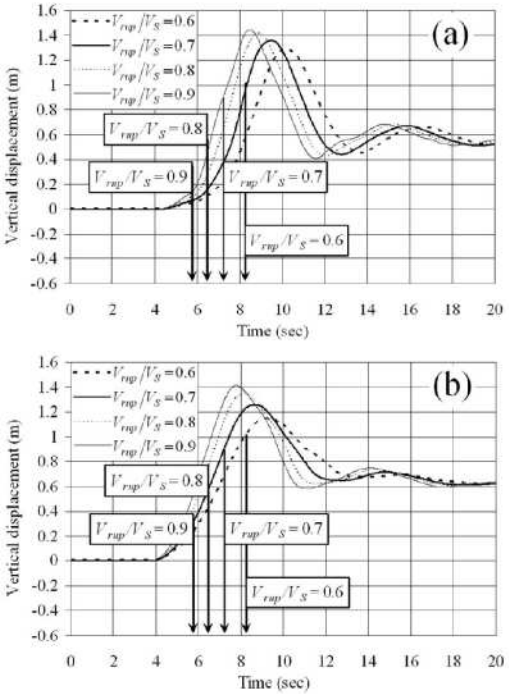

Fig. 2.7. Vertical ground surface displacement for different rupture velocities for (a) D_t = 300 m; (b) D_t = 5000 m. Arrows indicate the times ruptures end.

2.4. Rise time (case 4)

Figures 2.8 and 2.9 show the horizontal and vertical displacement of the soft layer surface at different locations for different rise time of fault slip.

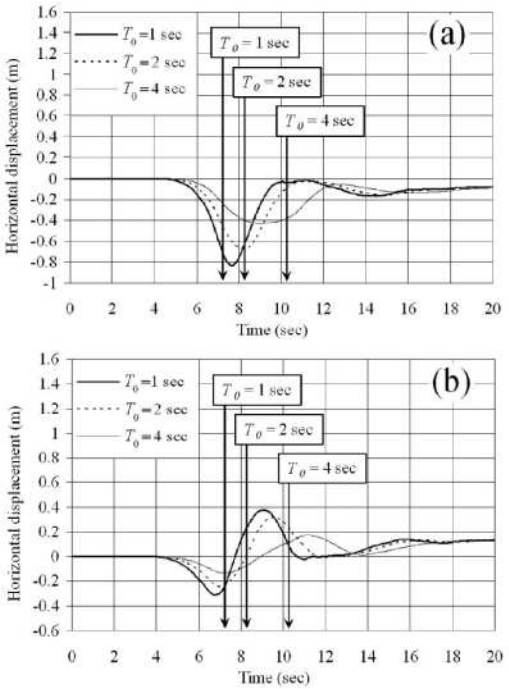

Fig. 2.8. Horizontal ground surface displacement for different rise times of fault slip for (a) D_t = 300 m; (b) D_t = 5000 m. Arrows indicate the times ruptures end.

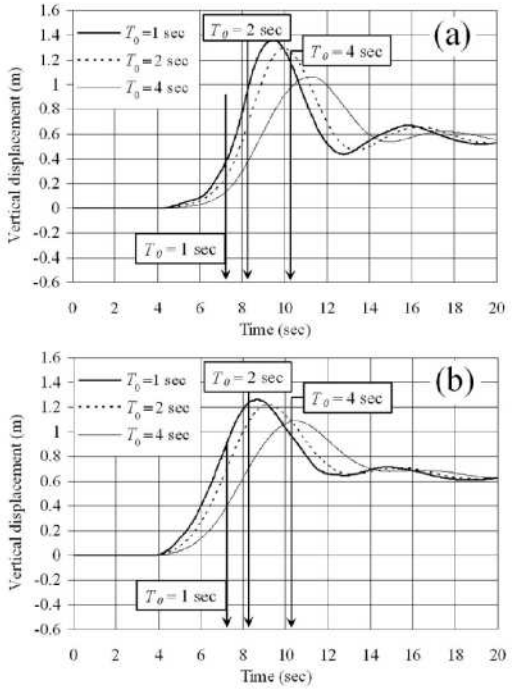

Fig. 2.9. Vertical ground surface displacement for different rise times of fault slip for (a) D_t = 300 m; (b) D_t = 5000 m. Arrows indicate the times ruptures end.

2.5. Final depth of fault tip (case 5)

Figures 2.10 and 2.11 show the horizontal and vertical displacement of the soft layer surface at different locations for different locations of final depth of fault tip.

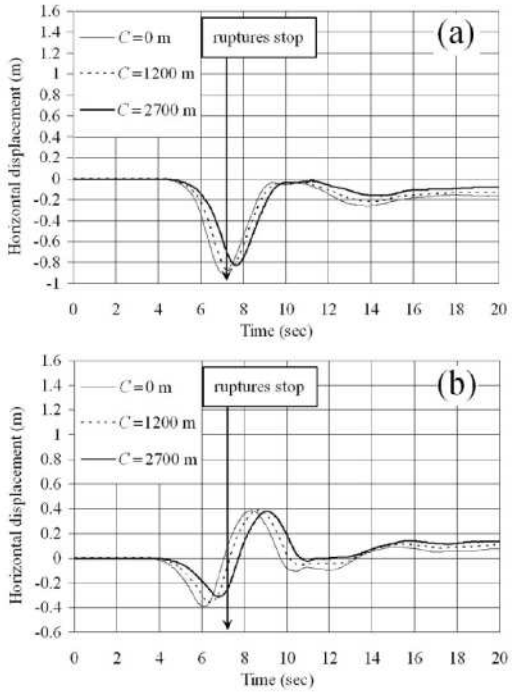

Fig. 2.10. Horizontal ground surface displacement for different locations for final depth of fault tip for (a) D_t = 300 m; (b) D_t = 5000 m. Arrow indicates the time ruptures end.

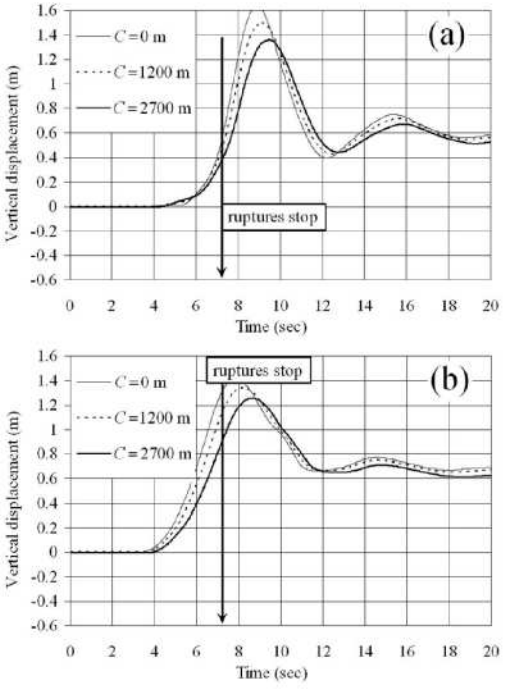

Fig. 2.11. Vertical ground surface displacement for different locations for final depth of fault tip for (a) D_t = 300 m; (b) D_t = 5000 m. Arrow indicates the time ruptures end.

2.6. Soft layer thickness (case 6)

Figures 2.12 and 2.13 show the horizontal and vertical displacement of the soft layer surface at different locations for different soft layer thicknesses.

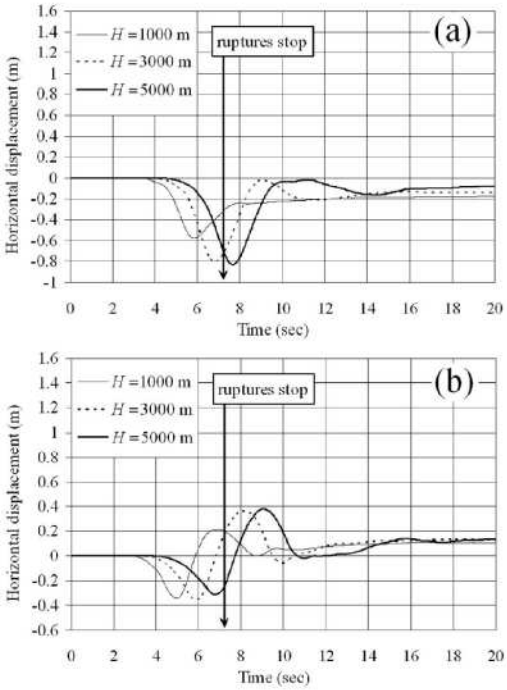

Fig. 2.12. Horizontal ground surface displacement for different soft soil thicknesses for (a) D_t = 300 m; (b) D_t = 5000 m. Arrow indicates the time ruptures end.

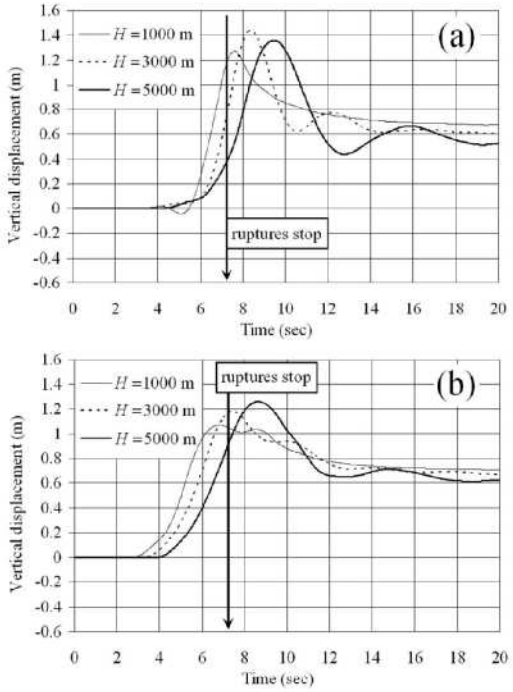

Fig. 2.13. Vertical ground surface displacement for different soft soil thicknesses for (a) $D_t = 300$ m; (b) $D_t = 5000$ m. Arrow indicates the time ruptures end.

2.7. Fault propagation direction (case 7)

Figures 2.14 and 2.15 show the horizontal and vertical displacement of the soft layer surface at different locations for different fault propagation directions.

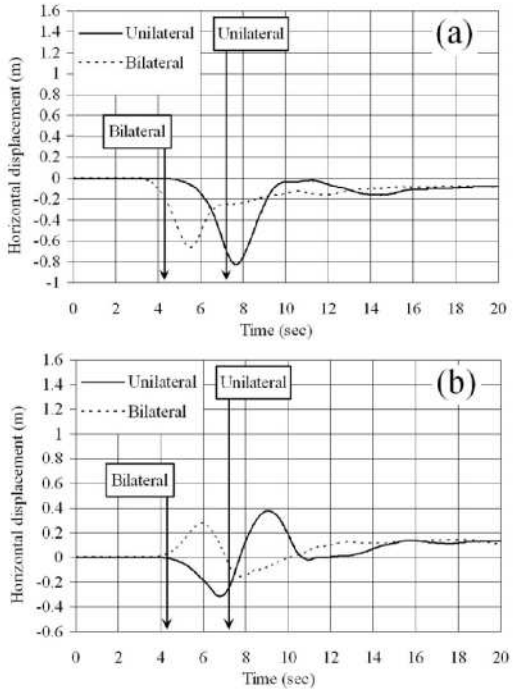

Fig. 2.14. Horizontal ground surface displacement for different fault propagation directions for (a) $D_t = 300$ m; (b) $D_t = 5000$ m. Arrows indicate the times ruptures end.

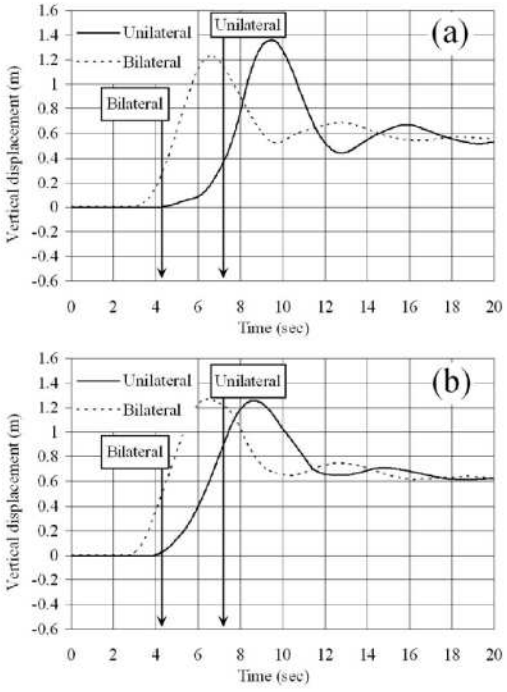

Fig. 2.15. Vertical ground surface displacement for different fault propagation directions for (a) $D_t = 300$ m; (b) $D_t = 5000$ m. Arrows indicate the times ruptures end.

2.8. Conclusions

As we can see from Fig. 2.2 to Fig. 2.15, in all cases horizontal and vertical surface displacement close to final location of fault tip starts with a motion toward footwall and upward, respectively. Farther seismograms have better resolution for detecting dip-slip angle comparing to other fault source parameters. Dip-slip angle has considerable effect on both horizontal and vertical displacement in a layered medium, but for other fault source parameters, horizontal displacement is more sensitive than vertical displacement. Dip-slip angle and final depth of fault tip have more effect on vertical surface displacement comparing to other fault source parameters. Except propagation direction parameter, in all other cases in the projected region above faulting area, horizontal displacement starts with a motion towards footwall and then hanging wall.

3. Effects of fault source parameters on the response of a circular tunnel

In this part, fault rupturing during strong ground motion is simulated and the effects of faulting on a nearby circular tunnel surrounded by a soft soil are studied using the finite element technique. In the near fault region, depending on the distance from the source, very complex wave patterns are produced, where the body and Rayleigh waves on the ground surface are neither well separated nor plane. The fault source parameters which are considered during this study are dip-slip angle θ, rupture velocity V_{rup}, rise-time of the fault slip T_0, final depth of fault tip H and the permanent slip $\delta = 1$ m. The effects of these parameters

on displacement field in the near fault region and ovallity factor of the tunnel which represents the deformation of the tunnel relative to its original shape are investigated. Finally the maximum hoop stress inside the concrete lining is plotted. The ovallity factor together with internal forces of the tunnel can be used to predict or quantify damage to tunnels due to deformation.

Geometry of the problem, definitions of the parameters and material properties of the soil and concrete of the tunnel are depicted in Fig. 3.1, Fig. 3.2 and Table 3.1, respectively.

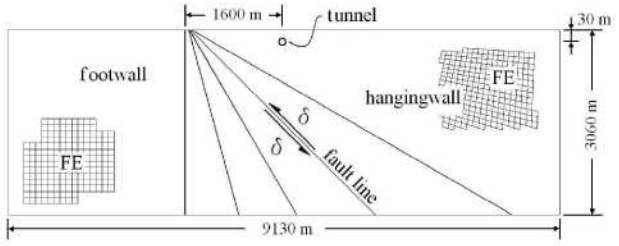

Fig. 3.1. Geometry of the medium consists of elastic half-space (FEM) including a concrete circular tunnel.

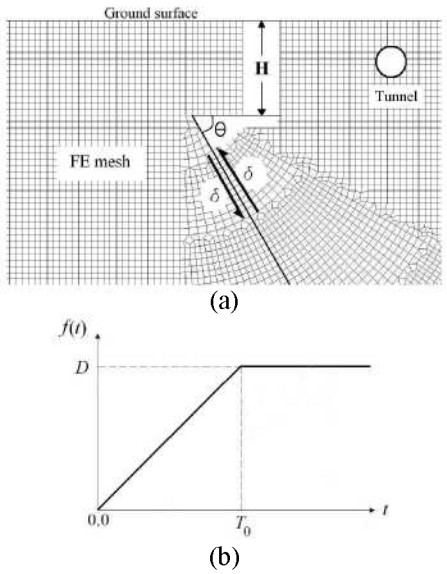

Fig. 3.2. Definitions of fault source parameters for (a) dip-slip angle θ, permanent slip δ, final depth of fault tip H; (b) rise time of the fault slip T_0.

Table 3.1
Material properties of the soil and concrete.

	υ	ρ (kg/m^3)	E (N/m^2)
Soil	0.4	1900	8.512E8
Concrete	0.15	2500	2.4E10

In all cases, default values for parameters are considered as follows unless they are expressed explicitly:

$\delta = 1$ m, $\theta = 45^\circ$, $V_{rup}/V_S = 0.75$, $T_0 = 1$ sec, $H = 0$ m.

Table 3.2 shows the values of fault source parameters in each case.

Table 3.2
Values for each fault source parameter.

Case No.	Values
1	$\theta = 30^\circ,\ 45^\circ,\ 60^\circ,\ 75^\circ,\ 90^\circ$
2	$V_{rup}/V_S = 0.65,\ 0.75,\ 0.85$
3	$T_0 = 1,\ 2,\ 3$ sec
4	$H = 0,\ 500,\ 1000$ m

For all cases, ovallity factor of the tunnel is calculated. Ovallity factor is defined as $\beta = a/b$, where a and b are the maximum and minimum deformed diameters of the tunnel. The ovallity factor together with internal forces of the tunnel makes the future study possible to predict damage to the tunnel during a near fault strong ground motion. Following parts show the effects of each parameter on ovallity factor of the circular tunnel.

3.1. Dip-slip angle (case 1)

Figure 3.3 shows the time variation of ovallity factor of the circular tunnel for different dip-slip angles.

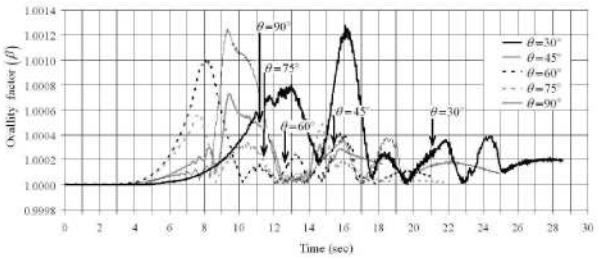

Fig. 3.3. Time variation of ovallity factor of the tunnel for different dip-slip angle.

For $\theta = 45^\circ$, the displacement amplitude increment at $t = 9.34$ sec which corresponds to the maximum ovallity factor β, is plotted in Fig. 3.4. It can be seen that the maximum displacement amplitude increment is at the fault tip and is directed towards the tunnel. The response of the tunnel is due to the superposition of direct incident waves from the rupture and reflected waves from the ground surface.

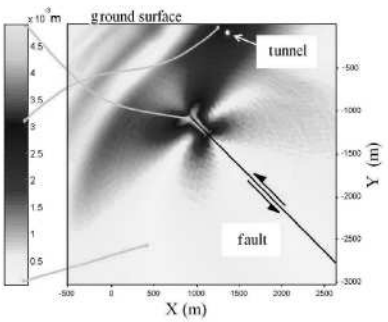

Fig. 3.4. Incremental displacement amplitude for $\theta = 45^\circ$, $V_{rup}/V_s = 0.75$ and $T_0 = 1$ sec.

3.2. Rupture velocity (case 2)

Figure 3.5 shows the time variation of ovallity factor of the circular tunnel for different rupture velocities.

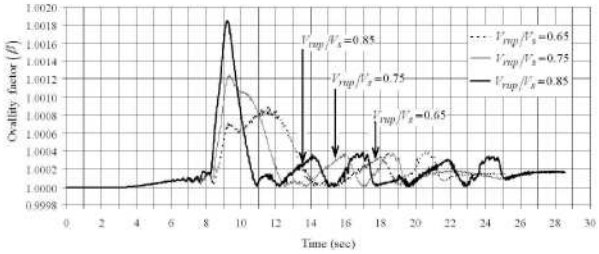

Fig. 3.5. Time variation of ovallity factor of the tunnel for different rupture velocities.

In this section, the effect of rupture velocity on hoop stress is investigated, where the prescribed parameters are $\theta = 45^{\circ}$, $H = 0.0$ m and $T_0 = 1$ sec. The maximum hoop stress is shown in Fig. 3.6 for $V_{rup}/V_s = 0.65,\ 0.75$ and 0.85. It shows that fast rupturing can cause higher hoop stress in tunnels.

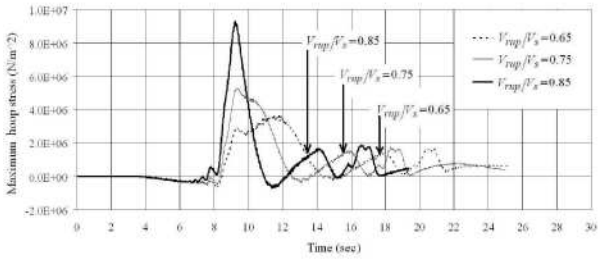

Fig 3.6. Maximum hoop stress for different rupture velocities, where $\theta = 45^{\circ}$, $H = 0.0$ m and $T_0 = 1$ sec. Arrows indicate the time rupture ends.

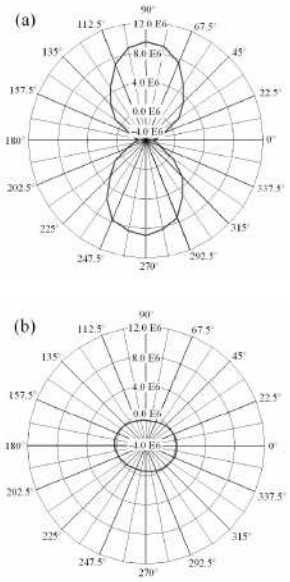

Fig. 3.7. Angular distribution of maximum hoop stress (N/m^2), where $\theta = 45^{\circ}$, $H = 0.0$ m, $V_{rup}/V_s = 0.75$ and $T_0 = 1$ sec for: (a) t = 9.24 sec; (b) t = 11.39 sec; (c) t = 14.19 sec.

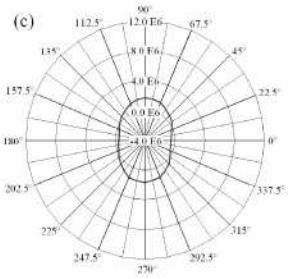

Fig. 3.7. Continued

Figure 3.7 shows the hoop stresses inside the lining at t = 9.24, 11.39, and 14.19 sec, which correspond to the first three maximum and minimum values of the hoop stress.

Combining internal forces (hoop stresses) with deformation of the lining (ovallity factor) makes the prediction of a tunnel failure possible during a strong ground motion.

3.3. Rise time (case 3)

Figure 3.8 shows the time variation of ovallity factor of the circular tunnel for different rise times.

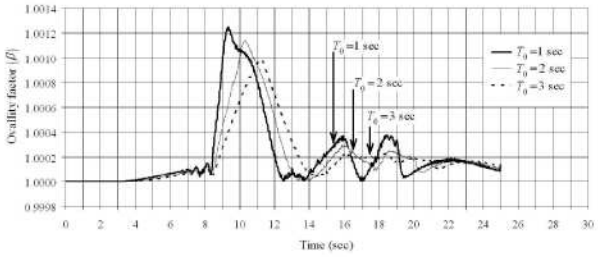

Fig. 3.8. Time variation of ovallity factor of the tunnel for different rise times.

3.4. Final depth of the fault tip (case 4)

Figure 3.9 shows the time variation of ovallity factor of the circular tunnel for different locations of the final depth of the fault tip.

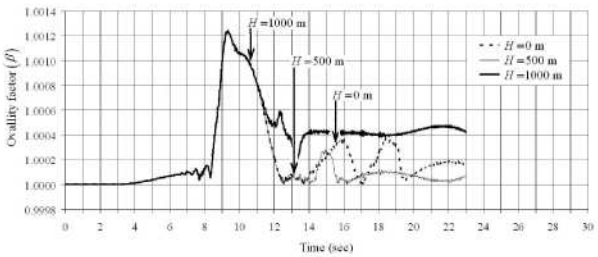

Fig. 3.9. Time variation of ovallity factor of the tunnel for different locations of the final depth of the fault tip.

In order to interpret this behaviour, the displacement field around the rupture tip is investigated. For instance at t = 16 sec around the rupture tip, the displacement field is non-uniform, but on either side of the rupture line the displacement field becomes uniform away from the rupture tip (Fig. 3.10a-c). If the rupture stops near the tunnel, this non-uniform displacement field applies permanent non-uniform deformation to the tunnel.

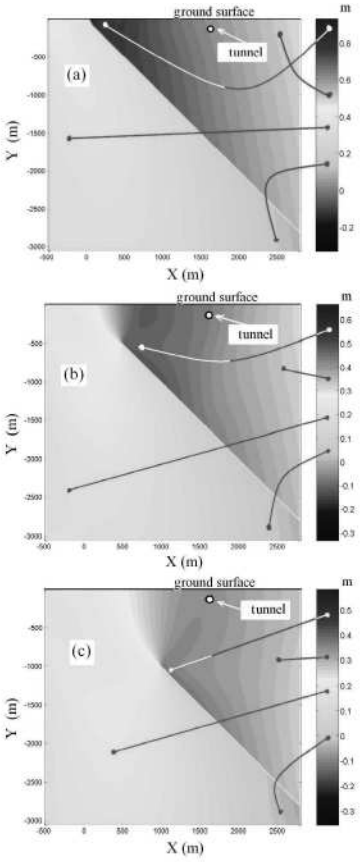

Fig. 3.10. Vertical displacement component u_y near the fault tip at $t = 16$ sec, for (a) $H = 0$ m; (b) $H = 500$ m; (c) $H = 1000$ m.

3.5. Conclusions

Among the fault source parameters, dip-slip angle and rupture velocity have more effect on ovallity factor of a circular tunnel than rise-time and final depth of fault tip. Shorter rise-time produces high frequency waves which increase the ovallity factors of tunnels. If the fault stops near a tunnel, the non-uniform displacement field around the fault tip applies permanent non-uniform deformation to the tunnel. Fast rupturing applies more deformation and internal forces to tunnels than slow rupturing.

Appendix

In the split–node technique (Melosh and Raefsky 1981) the fault slip is simulated by forces which are applied on fault elements and produce the same amount of displacements in the medium as the actual rupture. Fault elements are the elements which have at least one shared node on the fault line (shaded elements in Fig. A.1). For simplicity only one element on each side of the fault line is depicted in Fig. A.2. The geometry of the two elements at time t has been shown by dashed lines IMNJ and MKLN. From time t to $t+\Delta t$, the left and right elements move to the new locations I′M′N′J′ and M′K′L′N′, and nodes M′ and N′ split virtually. The displacement of node M in the left and right elements at $t+\Delta t$ are calculated by ${}_{\mathrm{L}}\mathrm{U}_{\mathrm{M}} = \langle \mathrm{U}_{\mathrm{M}} \rangle + \Delta \mathrm{U}_{\mathrm{M}}$ and ${}_{\mathrm{R}}\mathrm{U}_{\mathrm{M}} = \langle \mathrm{U}_{\mathrm{M}} \rangle - \Delta \mathrm{U}_{\mathrm{M}}$, where $\langle \mathrm{U}_{\mathrm{M}} \rangle$ is the displacement mean value of the node M′ relative to M, which is calculated from solving the complete system of the equations of motion together with relevant boundary conditions, and $\Delta \mathrm{U}_{\mathrm{M}}$ is the input relative slip of the elements at node M′ at $t+\Delta t$. Using the same definition, the displacement of node N in the left and right elements at $t+\Delta t$ can be calculated.

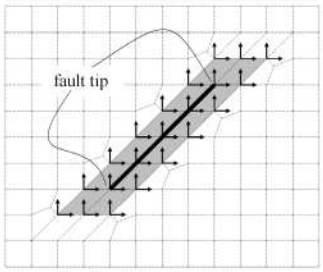

Fig. A.1. Nodal forces applied on fault elements in split-node technique.

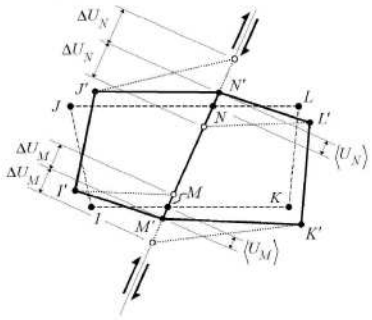

Fig. A.2. Deformations of fault elements on both sides of fault line after applying split-node forces.

Thus, by calculating the new locations of the nodes and the stiffnesses of fault elements, the induced forces at the nodes of the fault elements due to the slip can be calculated. To simulate propagation of the rupture, the split-node forces can be applied with time delay along the fault line. The relative slips and hence equivalent split-node forces reach the final values according to the prescribed slip function.

References

1) Liu, G. R., and Y. T. Gu (2001). A point interpolation method for two-dimensional solids, *Int. J. Num. Meth. Eng.* 50, 937–951.
2) Liu, G. R., and Y. T. Gu (2005). *An introduction to meshfree methods and their programming*, Springer.
3) Lysmer, J., and R. L. Kuhlmeyer (1969). Finite dynamic model for infinite media, *J. Eng. Mech. Div. ASCE* 95, 859–877.
4) Melosh, H. J., and A. Raefsky (1981). A simple and efficient method for introducing faults into finite element computations, *Bull. Seism. Soc. Am.* 71, 1391–1400.